



## Assistance of rearrangement of active sites in Fe/N/C catalyst for harvesting ultra-high power density PEMFCs

Yongkang Wu<sup>a</sup>, Mengchen Yuan<sup>a</sup>, Xiaoke Li<sup>a</sup>, Rui Ding<sup>a</sup>, Xiao Duan<sup>a</sup>, Jia Li<sup>a,\*</sup>, Ying Wang<sup>c,\*</sup>, Xiaolin Li<sup>c</sup>, Yunbo Zhang<sup>c</sup>, Jianguo Liu<sup>b,\*</sup>

<sup>a</sup> National Laboratory of Solid State Microstructures, College of Engineering and Applied Sciences, and Collaborative Innovation Center of Advanced Microstructures, Nanjing University, 22 Hankou Road, Nanjing 210093, China

<sup>b</sup> Energy and Power Innovation Research Institute, North China Electric Power University, 2 Beinong Road, Beijing 102206, China

<sup>c</sup> China Automotive Innovation Corporation, 88 Shengli Road, Nanjing 211106, China



### ARTICLE INFO

#### Keywords:

Rearrangement  
Active sites  
Fe/N/C Catalyst  
PEMFCs  
Power Density

### ABSTRACT

The infeasible cost of PEMFCs can be effectively lowered by replacing Pt-based catalysts with PGM-free catalysts. Although promising advancements have been achieved recently, the practical availability of PGM-free catalysts in PEMFCs remains apprehensive, typically, owing to their low output power density. Herein, a huge breakthrough has been made for high power density PGM-free PEMFCs with a peak power density of 1.36 W cm<sup>-2</sup> in H<sub>2</sub>-O<sub>2</sub> and 0.65 W cm<sup>-2</sup> in H<sub>2</sub>-air PEMFCs. Moreover, after iR-corrected, it delivers an affirmative current density of 62 mA cm<sup>-2</sup> at 0.9 V in H<sub>2</sub>-O<sub>2</sub> fuel cells, a breakthrough on the US Department of Energy 2025 target for PGM-free catalysts. The tremendous progress can be attributed to the rearrangement of active sites by recrystallization which significantly increases the active site density and mesoporosity of the Fe/N/C catalyst. Consequently, it cost-effectively enhances the catalytic activity and boosts its power density output.

### 1. Introduction

As a highly efficient energy conversion device, a polymer electrolyte membrane fuel cell (PEMFCs) is demanded worldwide owing to its pure zero-pollutant emission, typically, application in transport vehicles [1–4]. However, infeasible cost makes it a dominant problem bearing practical significance of PEMFC for further development. Reducing and completely replacing noble platinum group metal (PGM) catalysts are the essential solutions for decreasing the total stack cost, 40% of which comprises the PGM catalyst [5,6]. Continuous efforts have been made for realizing high-catalytic activity PGM-free catalysts, principally M/N/C (where M = Fe, Co, Mn) materials. Especially, in terms of half-wave potential, some of them present values even comparable to those of PGM-based catalysts in alkaline or sulfuric acid system rotating disk electrode (RDE) assessment [7–9]. However, when assembled practically in PEMFCs, the actual power density outputs of PGM-free catalysts are far from those of PGM-based catalysts [3]. Considering the above, the US Department of Energy (DOE) has equally set five-year periodical targets for PGMs free membrane electrode assemblies (MEA),

representatively, an activity of 44 mA cm<sup>-2</sup> at 0.90 V<sub>iR</sub>-free as the 2025 target [10].

Over the years, there has been tremendous progress in realizing high-activity PGM-free catalysts and attempts have been made to promote their practical application in PEMFCs [11]. Single-atom catalysts (SACs) exhibit the unique superiority of nearly 100% utilization of catalytic active sites [12,13]. Particularly, zeolitic imidazolate framework (ZIF)-derived single iron atoms embedded in nitrogen-doped carbon framework catalysts have been generated significant interest and are considered as the most promising cathode catalysts to produce high-power density PGM free PEMFCs owing to their high oxygen reduction reaction (ORR) activity [14–16]. Wu and co-workers [17] established high-performance PEMFCs cathode catalysts with controllable density of atomically dispersed iron active sites by turning the doped Fe content in ZIF-8 precursors. The results showed that an effective route to enhance the catalytic activity of Fe/N/C catalysts is to increase the Fe content to the maximum extent on the premise that no iron clusters are generated. Subsequently, numerous studies have been conducted to increase the density of Fe/N/C active sites [18,19]. In

**Abbreviations:** PEMFCs, Polymer electrolyte membrane fuel cells.

\* Corresponding authors.

E-mail addresses: [lijia0226@nju.edu.cn](mailto:lijia0226@nju.edu.cn) (J. Li), [wangying@t3caic.com](mailto:wangying@t3caic.com) (Y. Wang), [jianguoliu@ncepu.edu.cn](mailto:jianguoliu@ncepu.edu.cn) (J. Liu).

<https://doi.org/10.1016/j.apcatb.2022.121365>

Received 21 February 2022; Received in revised form 25 March 2022; Accepted 30 March 2022

Available online 9 April 2022

0926-3373/© 2022 Elsevier B.V. All rights reserved.

addition to increase the active sites density, Mazzucato et al. [20] directly verified that the derived micro- and mesoporous structures of carbon supports also play important roles in catalytic site formation and activity. For example, an open structure benefits the deposition of more active sites and better access to active sites than a closed one. From this perspective, the Shui's group [21] designed high efficient Fe/N/C catalysts with dense active sites and enhanced mesoporosity for practical application and achieved a high peak power density of  $1.18 \text{ W cm}^{-2}$  and a current density of  $47 \text{ mA cm}^{-2}$  at  $0.88 \text{ V}$ . This value satisfies the DOE 2018 activity target of PGM-free catalysts. Likewise, Zhou and co-workers [22] reported a carboxylate-assisted strategy to enhance the active site density and mesoporosity of Fe/N/C catalysts and found that when assembled in PEMFCs, it achieves a new record of peak power density of  $1.33 \text{ W cm}^{-2}$  among PGM-free catalysts. More recently, Li et al. [23] achieved a further breakthrough and accomplished a current density output of  $33 \text{ mA cm}^{-2}$  @  $0.9 \text{ V}_{\text{IR-corrected}}$  with high-catalytic activity Fe/N/C materials formed by the chemical vapor deposition method. Although promising achievements have been realized for PGM-free catalysts, the performance of PGM-free MEA is still in an awkward situation to meet practical targets, e.g., a current density of  $44 \text{ mA cm}^{-2}$  @  $0.9 \text{ V}_{\text{IR-corrected}}$  set by DOE. Moreover, further progress and practical application methods to boost the performance of Fe/N/C catalyst in PEMFCs remain in extremely urgent.

In this study, we developed a suitable rearrangement strategy for active sites by disorder and recrystallization treatments of Fe-doped ZIF (Fe-ZIF) precursor followed by a direct pyrolysis process to produce high-catalytic activity Fe/N/C catalysts. After rearrangement, both the active site density and mesoporosity of Fe/N/C catalyst were significantly enhanced, which was directly associated with the catalytic activity for the ORR and the power density output of the PEMFCs. As a consequence, when assembled finely in a PEMFC cathode, the Fe/N/C catalyst with rearrangement of active sites delivered an excellent performance with a new recorded peak power density of  $1.36 \text{ W cm}^{-2}$  in  $\text{H}_2\text{-O}_2$  and  $0.65 \text{ W cm}^{-2}$  in  $\text{H}_2\text{-air}$  PEMFCs. Moreover, after iR-corrected, it presented a favorable current density of  $62 \text{ mA cm}^{-2}$  at  $0.9 \text{ V}$  in  $\text{H}_2\text{-O}_2$  PEMFCs, a breakthrough for realizing the DOE 2025 target for PGM free catalysts.

## 2. Experimental section

### 2.1. Synthesis of ZIF-8 nanoparticles

ZIF-8 nanoparticles are synthesized by a hydrothermal method. Typically, 10,512 mg 2-mlm and 9520 mg  $\text{Zn}(\text{NO}_3)_2\cdot 6 \text{ H}_2\text{O}$  were dissolved in 120 mL and 240 mL MeOH solution respectively. After adequately stirring, put the latter solution into the former one and stirring acutely for another 1 h. Then add the obtained white emulsion into Teflon lined stainless steel reactor with each kettle loading 30 mL solution and put the reactor into drying oven with the setup of  $120^\circ\text{C}$  for 4 h. Finally, ZIF-8 nanoparticles were collected after repeated centrifugation, cleaning and drying.

### 2.2. Synthesis of Fe-ZIF nanoparticles with disorder and rearrangement treatments

2000 mg ZIF-8, 500 mg 1,10-phenanthroline (phe) and 25 mg  $\text{Fe}(\text{Ac})_2$  (at mass ratio of 80:20:1) were added into a mixture of 100 mL MeOH and 20 mL  $\text{H}_2\text{O}$  and stirring adequately. Evaporating solvent completely at  $85^\circ\text{C}$  accompanied by stirring and Fe-ZIF nanoparticles were collected after repeated washing, centrifugation and drying. Disordered Fe-ZIF (Fe-ZIF-Ball) powders were obtained after a ball-milling procedure (Nanjing NanDa Instrument Plant) with a sample-to-ball weight ratio of 1:50 at 250 rpm for 8 h and the rearranged Fe-ZIF (Fe-ZIF-Recry) powders were gained after an extra recrystallization treatment of completely stirring of the Fe-ZIF-Ball in MeOH solution for 1 h.

### 2.3. Synthesis of Fe/N/C catalysts with disorder and rearrangement treatments

A one-step pyrolysis condition of  $1000^\circ\text{C}$  for 1 h was adopted to obtain Fe/N/C catalysts and the obtained catalysts with different precursors were recorded as Fe/N/C, Fe/N/C-Ball and Fe/N/C-Recry, correspondingly.

### 2.4. Electrocatalytic performance tests

Oxygen reduction reaction (ORR) activity of as prepared catalysts was evaluated by the polarization curves carried out with a conventional three compartment electrochemical cell in  $\text{O}_2$ -saturated 0.1 M  $\text{HClO}_4$  at  $25^\circ\text{C}$ , 1600 rpm,  $10 \text{ mV s}^{-1}$  from 0 to  $1.2 \text{ V}$ . Glassy carbon electrode (GC,  $0.019625 \text{ cm}^2 \text{ SA}$ ), graphite electrode (GE) and reversible hydrogen electrode (RHE) were selected as the working electrode, counter electrode and reference electrode, respectively. The catalyst ink was obtained after a sufficient ultrasonic dispersion of slurry containing 6 mg catalyst in a mixture solution of 0.43 mL  $\text{H}_2\text{O}$ , 0.43 mL IPA and 0.053 mL nafton (5 wt%, E.W. 10000), and then deposited dropwise on a GC electrode until a 0.6 mg  $\text{cm}^{-2}$  catalyst loading was received. Cyclic voltammetry (CV) test (0–1.2 V,  $50 \text{ mV s}^{-1}$ ) was performed primarily on an electrochemical workstation (CHI 760) equipped with a modulated speed rotator (Pine Instruments, CPR+Wavenow) to activate and stabilize the catalyst. After full activation and stabilization, the polarization curves were conducted upon potential cycling in the range of 0–1.2 V with ohmic compensated in  $\text{O}_2$ -saturated 0.1 M  $\text{HClO}_4$  electrolyte at  $25^\circ\text{C}$  at a spinning rate of 1600 rpm.

### 2.5. Active site density (SD) tests

The SD values were calculated by generally accepted nitrite reduction stripping measurements including cleaning protocol, measurement protocol, and poisoning protocol. [24,25] Briefly, an active  $\text{Fe-N}_x$  site can adsorb tightly of five NO to form a stable component, which consequently poisoned the ORR performance of catalyst. However, the adsorbed NO can be stripped at the potential of  $-0.3 \text{ V}$ . Therefore, the number of  $\text{Fe-N}_x$  active sites can be calculated according to the stripped molecules i.e. the electrochemical nitrite reduction stripping charge ( $Q_{\text{strip}}$ ). Specific calculation formulas for the areal-based site density ( $SD_{\text{BET}}$ ) and mass-based site density ( $SD_{\text{mass}}$ ) were shown as follows:

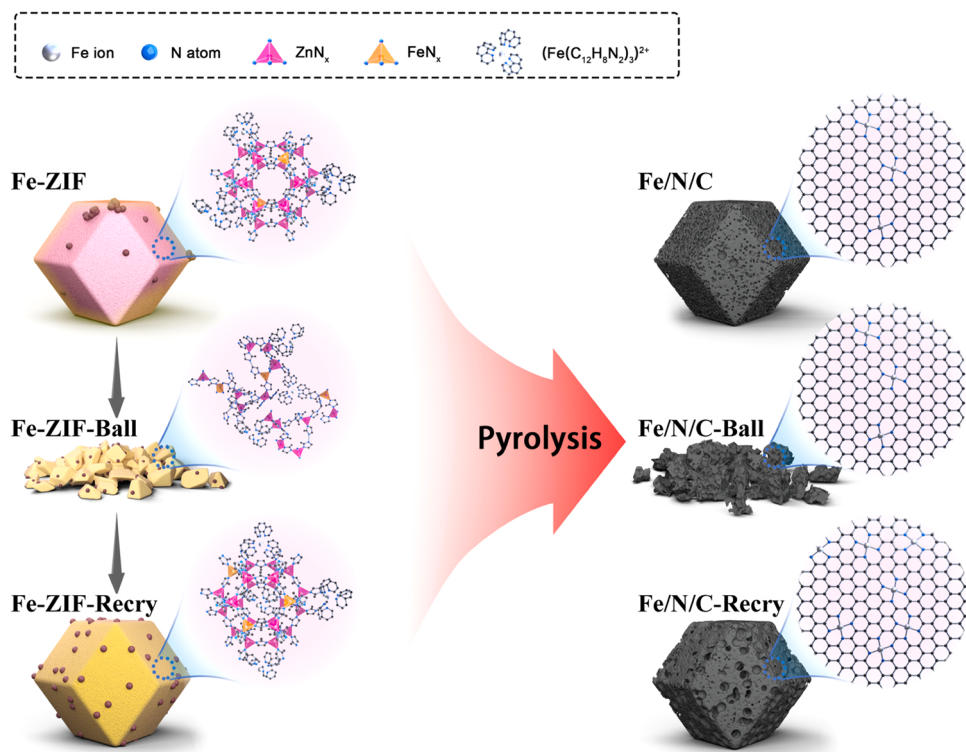
$$SD_{\text{BET}} \text{ (NO}_2^-\text{)} \text{ [site nm}^{-2}\text{]} = \frac{Q_{\text{strip}} \times N_A}{n_{\text{strip}} \times F \times A_{\text{BET}} \times m_{\text{cat}}} \quad (1)$$

$$SD_{\text{mass}} \text{ (NO}_2^-\text{)} \text{ [site g}^{-1}\text{]} = \frac{Q_{\text{strip}} \times N_A}{n_{\text{strip}} \times F \times m_{\text{cat}}} \quad (2)$$

Where  $Q_{\text{strip}}$  is the coulomb charge relevant to the NO stripping reaction,  $n_{\text{strip}}$  (the value here is 5) is the electron transfer numbers of one SD,  $A_{\text{BET}}$  is the specific surface area of catalyst and  $m_{\text{cat}}$  is the mass of catalyst coated on the GC. Prior to measurements, all catalysts were disposed by 0.5 M  $\text{H}_2\text{SO}_4$  solution at  $60^\circ\text{C}$  to remove any potential impurities (e. g. Fe clusters) that may influence the value of electrochemical nitrite reduction stripping charge.

### 2.6. Membrane electrode assembly (MEA) preparation and fuel cell tests

In this paper, the MEA was composed of Fe/N/C catalyst deposited gas diffusion layer (GDL, Freudenberg, 250  $\mu\text{m}$ ), commercial 50% Pt/C (Tanaka) catalyst deposited proton exchange membrane (Gore, 15  $\mu\text{m}$ ), polyethylene terephthalate (PET) and silicone gasket. An available MEA was obtained after a hot-pressing treatment of the above components for 3 min at  $140^\circ\text{C}$ , 6 MPa and stored in a constant temperature ( $25^\circ\text{C}$ ) and humidity (70% RH) box for later use. The catalyst ink was prepared by



**Scheme 1.** Schematic of intermediate compounds in synthesis process.

adding catalyst (anode by 200 mg Pt/C and cathode by 100 mg Fe/N/C) into a mixture of 2.174 mL 5 wt% Nafion solution, 7.629 mL IPA and 1.907 mL H<sub>2</sub>O and magnetically stirred for 24 h at 0 °C. Before ultrasonic spraying, catalyst ink was treated by an extra ultrasonic dispersion for 1 h at 0 °C. The loading of cathode and anode are controlled at 3 mg<sub>Fe/N/C</sub> cm<sup>-2</sup> and 0.1 mg<sub>Pt</sub> cm<sup>-2</sup>, respectively. The effective area of as prepared MEA was 2.5 cm \* 2.5 cm. Fuel cell performance were all measured at 80 °C with 100% RH of 300/300 sccm flow rates in H<sub>2</sub>/O<sub>2</sub> and 250/1000 sccm in H<sub>2</sub>/Air atmosphere via a fuel cell test system (Module 850e, Scribner Associates Inc.) equipped with a potential station (Module 885, Scribner Associates Inc.). Back pressure of 2 bar was used. Specifically, the polarization curves in H<sub>2</sub>/Air atmosphere were collected after three cycles in H<sub>2</sub>/O<sub>2</sub>.

### 3. Results and discussion

#### 3.1. Catalysts synthesis

The experimental process was illustrated in **Scheme 1**. First, an Fe-ZIF precursor was synthesized through a general wet-impregnation method using precursors Fe(Ac)<sub>2</sub>, 1,10-phenanthroline and ZIF-8. A Two-step treatment of disorder by ball-milling and rearrangement by recrystallization was applied sequentially to the Fe-ZIF precursor. Especially, the ball-milling treatment was implemented for two reasons. One was because ball-milling technology is a simple approach for synthesizing functional materials with disordered meso- and macroporous defects and is applicable for large-scale yields [26]. The second reason was that the enormous energy adhered to ball-milling can straightly break the confined dodecahedral crystal framework of ZIF-8, which would be favorable for the subsequent rearrangement process. As reported, 1,10-Phenanthroline is an excellent precursor for pyridine nitrogen source and iron chelation [27]. However, the ZIF-8 skeleton only features large cavities of 11.6 Å [28], which are insufficient for iron chelation (tris (1,10-phenanthroline) iron (II), 14.96 Å) to penetrate [29]. Comparatively, the broken framework of ZIF-8 is adequate for iron chelation to penetrate and positively promotes the coordination of iron

ions with ZIF-8 and further conversion of ZnN<sub>x</sub> to FeN<sub>x</sub> clusters [30]. Therefore, after the following rearrangement treatment by recrystallization, we harvested an Fe-ZIF compound with both the dodecahedral restrictive framework of ZIF-8 (**Fig. 1c**) and enhanced coordination site density of iron ions with the skeleton of ZIF-8. Finally, a one-step pyrolysis process was conducted to obtain highly active Fe/N/C catalysts. For comprehensively investigate the function of the disorder and rearrangement treatment, we analyzed three treated Fe-ZIF precursor-derived Fe/N/C catalysts, denoted as Fe/N/C, Fe/N/C-Ball and Fe/N/C-Recry, respectively.

#### 3.2. Structural evolution characterization and mechanism analysis

First, the morphology and structure of the as synthesized Fe-ZIF precursors and pyrolysis-derived Fe/N/C catalysts were investigated, the results of which are shown in **Fig. 1a-f**. All pyrolysis-derived Fe/N/C catalysts maintained the general morphology of the corresponding Fe-ZIF precursor, indicating that pyrolysis process have a negligible effect on the intrinsic skeleton of all Fe-ZIF precursors. However, it is noteworthy that there are abundant wrinkles in Fe/N/C-Recry, as shown in **Fig. 1f** and the enlarged figures in **Fig. 1d-f**. Pore structures of the three catalysts were characterized by N<sub>2</sub> adsorption-desorption isotherm tests. As shown in **Fig. 1g**, the Fe/N/C catalyst exhibits a typical type-I isotherm of a microporous dominant structure with a maximum specific surface area of 1293 m<sup>2</sup> g<sup>-1</sup> (**Fig. S3**). In comparison, the Fe/N/C-Ball and Fe/N/C-Recry catalysts exhibit notable adsorption hysteretic isotherms of multistage distributed pore structures with specific surface areas of 893 m<sup>2</sup> g<sup>-1</sup> and 1015 m<sup>2</sup> g<sup>-1</sup>, respectively. Specifically, the Fe/N/C-Recry achieves the highest mesoporous volume ratio of 45.7% (**Fig. 1h**), which was supportive to the transmission electron microscopy (TEM) results. It's been reported by many researchers that a large proportion of active sites buried in ZIF-8-derived micropores are inaccessible and contribute finitely to the catalytic activity owing to the steric hindrance effect [20,31,32]. Therefore, the increase in induced mesoporosity is more favorable for boosting the catalytic activity of single iron atom-embedded N-C catalysts.

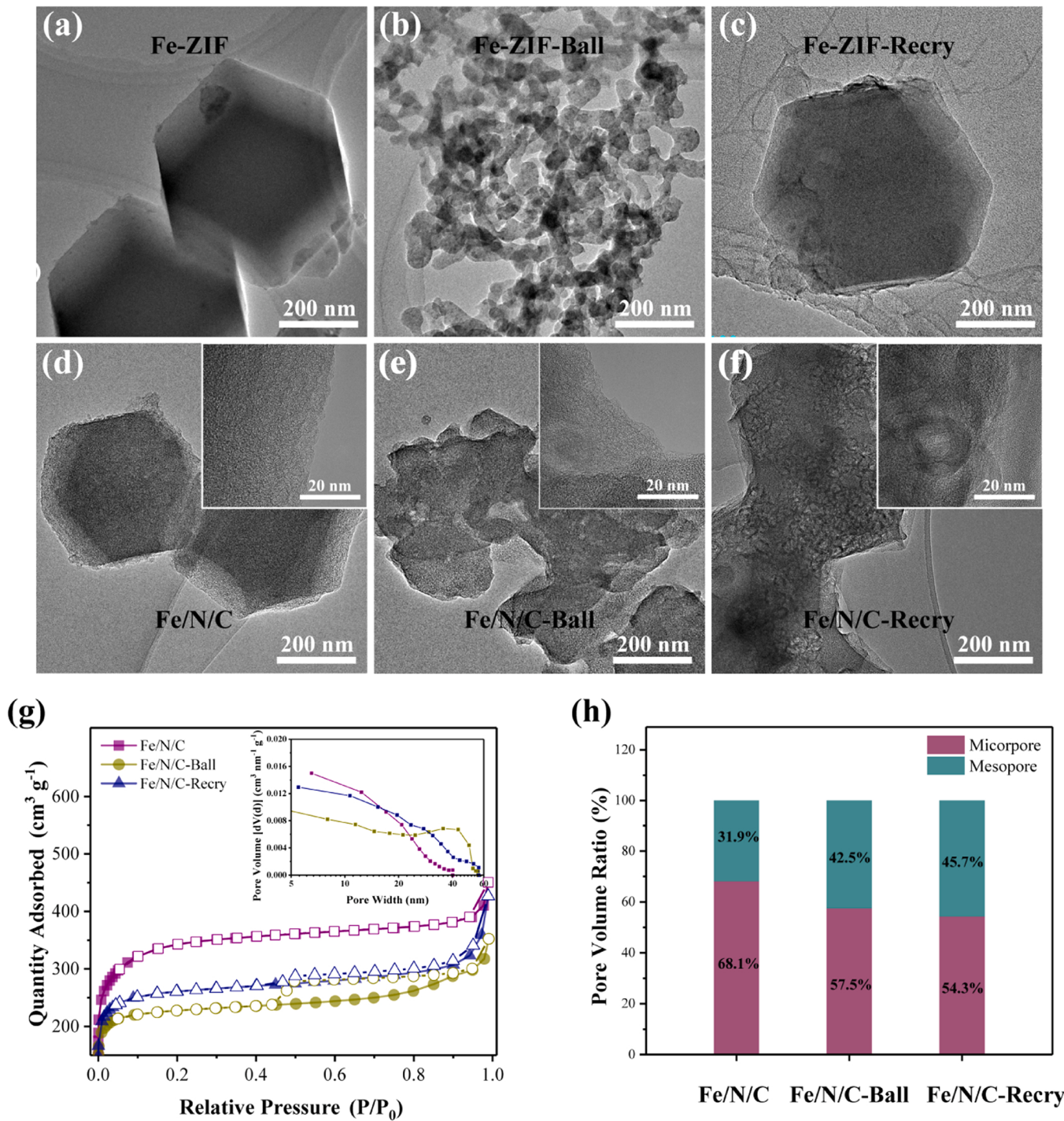


**Fig. 1.** TEM images of (a-c) Fe-ZIF, Fe-ZIF-Ball and Fe-ZIF-Recry, (d-f) Fe/N/C, Fe/N/C-Ball and Fe/N/C-Recry, respectively, (g)  $N_2$  adsorption and desorption isotherms (inset Graph: pore distributions curves calculated by Barrett-Joyner-Halenda method) and (h) micro- and mesoporous volume ratio of Fe/N/C, Fe/N/C-Ball and Fe/N/C-Recry.

In order to investigate the specific structural evolution process and mechanism of the enriched mesoporosity of the pyrolysis-derived Fe/N/C materials. X-ray diffraction (XRD) characterization was firstly conducted to verify the specific crystal structure transformation of the Fe-ZIF precursors after different treatments, and the results are shown in Fig. 2a. Apparently, the typical dodecahedral ZIF-8 crystal structure (JCPDS, 00-062-1030) [23] of Fe-ZIF precursor is completely disordered by ball-milling and subsequently recrystallized after the recrystallization treatment. Besides, the specific coordination conditions on the precursors and their derived catalysts were comparatively changed. As

shown in Fig. 2b, the specific peak at 3300–3500 cm<sup>-1</sup>, corresponding to the stretching vibration of N-H, moves towards a higher wavenumber after the ball-milling and recrystallization treatments. This is owing to the inductive effect of the electron-withdrawing groups [33], primarily -COOH and -C<sub>12</sub>H<sub>8</sub>N<sub>2</sub>, which can not only contribute to attracting more iron atoms around the N atoms of ZIF-8 framework but also act as pore-forming agents in the pyrolysis process [22]. As a consequence, it will enhance of the density of the Fe-N<sub>x</sub> cluster and mesoporosity in the subsequent pyrolysis process. Further testing by inductively coupled plasma-mass spectrometry (ICP-MS) showed that the mass ratio of iron

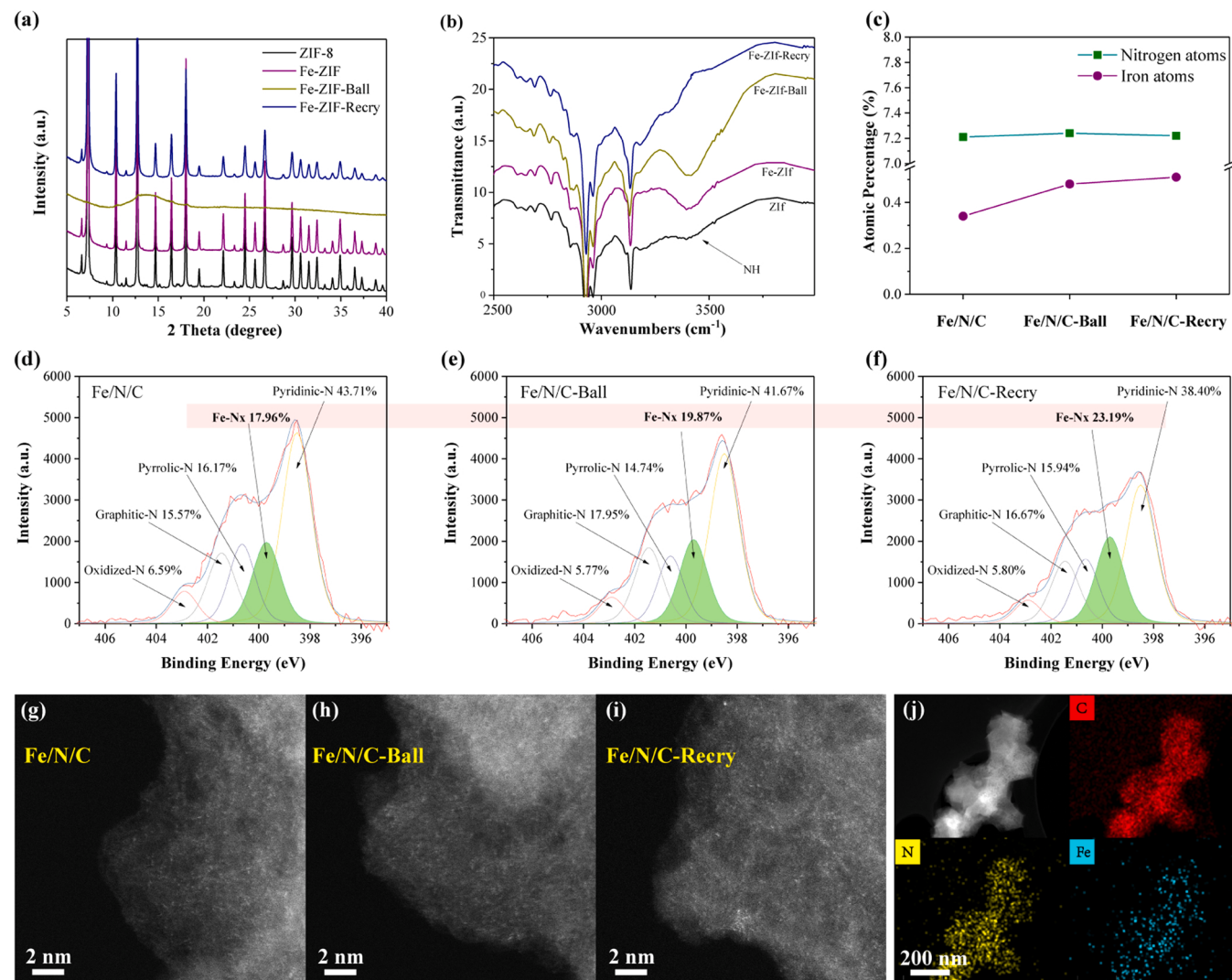


**Fig. 2.** Structural characterization. (a) XRD patterns and (b) FIRT spectra of Fe-ZIF precursors, (c) nitrogen and iron atomic percentages calculated by XPS, (d-f)  $\text{N}_{1s}$  spectra and (g-i) HAADF images of Fe/N/C, Fe/N/C-Ball and Fe/N/C-Recry, respectively. (j) EDS images of Fe/N/C-Recry.

in the three catalysts were 1.14%, 1.17% and 1.34% (Table S1), respectively, suggesting that the rearrangement treatment did slightly increase the content of iron in the catalysts. The results are in good agreement with our inferences. This approach of enhancing the density of the  $\text{Fe}-\text{N}_x$  clusters was further confirmed by X-ray photoelectron spectroscopy characterization. As shown in Fig. 2c, the total atomic content of nitrogen in Fe/N/C, Fe/N/C-Ball and Fe/N/C-Recry is approximately 7.2%, whereas the iron atomic content is gradually increased from 1.5% to 2.3%. Moreover, the  $\text{Fe}-\text{N}_x$  clusters are gradually increased from 17.96% to 23.19%, based on the subsequent calculation results of the  $\text{N}_{1s}$  spectra (Fig. 2d-f). It's worth noting that the  $\text{Fe}-\text{N}_x$  clusters are intrinsically relevant to catalytic active sites, as many studies have reported [34,35]. The increase in the  $\text{Fe}-\text{N}_x$  clusters can directly enhance the density of active sites and further boost the catalytic performance of the catalyst. The High-resolution transmission electron microscopy (Fig. S4a-d) images were collected to characterize the iron distribution status in all pyrolysis-derived materials, based on which no evident aggregation of iron particles was observed. According to high-angel annular dark-field microscopy (HAADF, Fig. 2g-i) images, we concluded that all iron atoms were distributed uniformly in a single atomic condition and coordinated well with nitrogen atoms (Fig. S5). In addition, a more uniform distribution of N and Fe elements was observed in Fe/N/C-Recry than in the other two, based on

energy-dispersive X-ray spectrums (EDS, Fig. 2j, Fig. S6 c and d). This indicates that rearrangement treatment assists the iron compounds in distributing more homogeneously.

Synchrotron-based X-ray absorption near-edge structure (XANES) and extended X-ray absorption fine structure (EXAFS) were performed to reveal further the coordination structures and chemical states of the three Fe/N/C catalysts. As shown in Fig. 3a-c, the spectral curves of the three Fe/N/C catalysts are almost identical, suggesting that the as-prepared three catalysts have the same coordination structure. The optimal fitting results of the three Fe/N/C catalysts are shown in Fig. 3d-f and Table S2 (Supporting Information). All three catalysts show a predominantly occupied peak at 1.41 Å, which is attributed to the Fe-N coordination in the first shell. The average coordination number (x) of the Fe/N/C, Fe/N/C-Ball and Fe/N/C-Recry samples were calculated to be 3.8, 3.9 and 4.0, respectively, indicating that all three catalysts have formed a square plane  $\text{Fe}-\text{N}_4$  structure.

### 3.3. Catalytic activity and active site density evaluation

The ORR activity was evaluated using the polarization curves obtained with a conventional three-compartment electrochemical cell in  $\text{O}_2$ -saturated 0.1 M  $\text{HClO}_4$  at 25 °C, 1600 rpm and 10 mV s<sup>-1</sup> from 0 V to 1.2 V. As shown in Fig. 4a, the Fe/N/C-Recry catalyst exhibits the

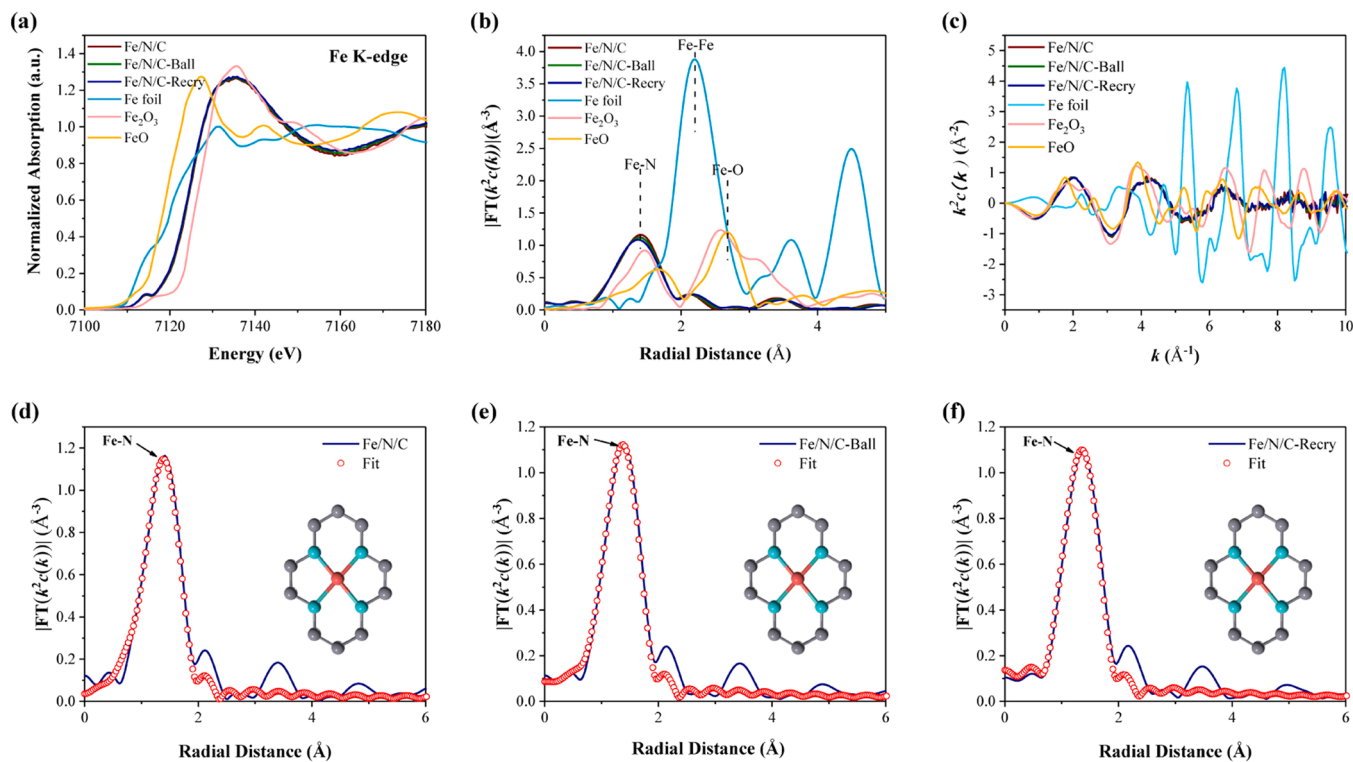


**Fig. 3.** (a) Fe K-edge XANES spectra, (b) FT-EXAFS curves and (c) E/K/R space spectra of Fe/N/C, Fe/N/C-Ball, Fe/N/C-Recry and standard compounds, (d-f) FT-EXAFS fitting curve of Fe/N/C, Fe/N/C-Ball and Fe/N/C-Recry, respectively.

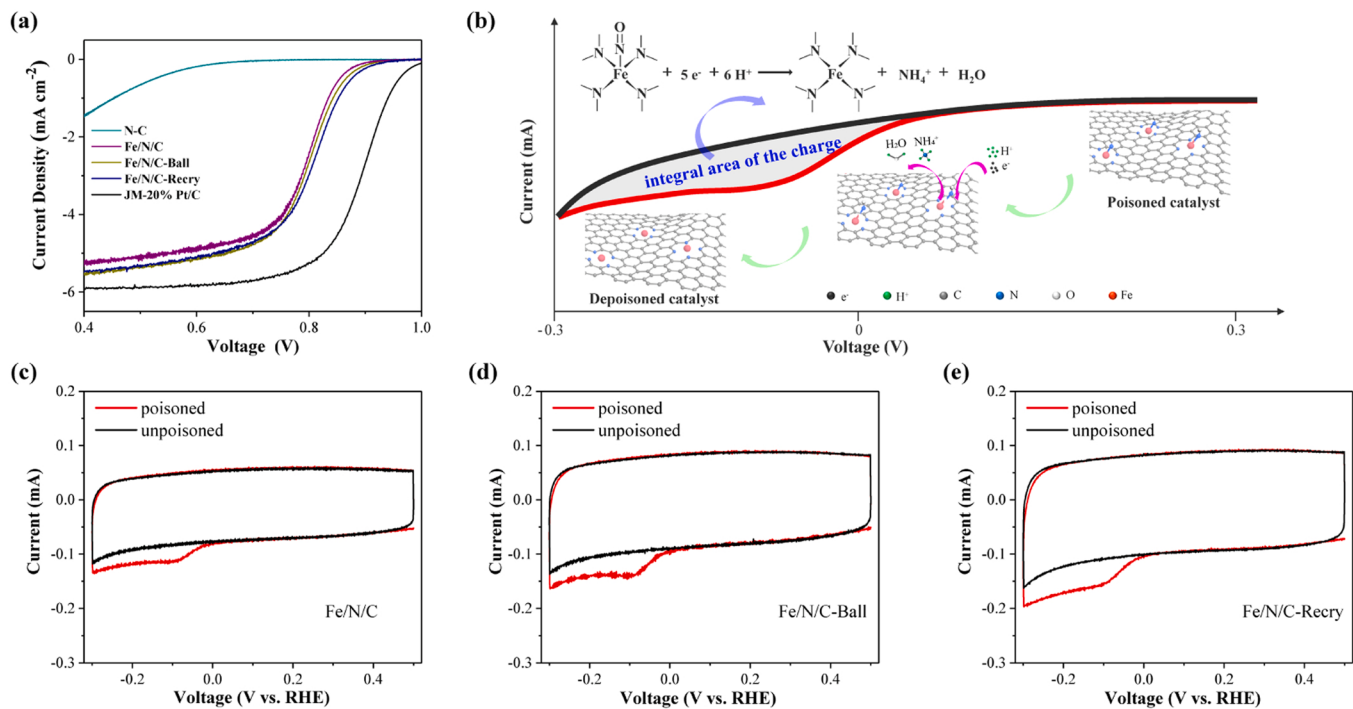


**Fig. 4.** (a) ORR linear sweeping voltammetry curves in  $O_2$ -saturated 0.1 M  $HClO_4$  solution with ohmic compensated at 1600 rpm and room temperature. All potentials mentioned versus reversible hydrogen electrode. (b-e) Active sites density measurements of Fe/N/C, Fe/N/C-Ball and Fe/N/C-Recry, respectively.

highest ORR activity with a half-wave potential of 0.806 V; in comparison, the Fe/N/C achieves it at 0.796 V and the Fe/N/C-Ball of 0.798 V, at a catalyst loading of  $0.6 \text{ mg cm}^{-2}$ . Subsequently, the density of active sites was evaluated based on a generally accepted nitrite reduction method [26,27], by which the number of  $\text{Fe}-\text{N}_x$  sites can be

equivalently quantified with the reversible adsorption and stripping charge of nitrite anions in cyclic voltammetry (CV) treatment. As shown in Fig. 4b-e, the Fe/N/C-Recry reveals the most abundant site density of  $2.8 \times 10^{19}$  sites/g of the catalyst, compared to the Fe/N/C of  $1.7 \times 10^{19}$  and Fe/N/C-Ball of  $2.4 \times 10^{19}$ . At this point, we demonstrated that the

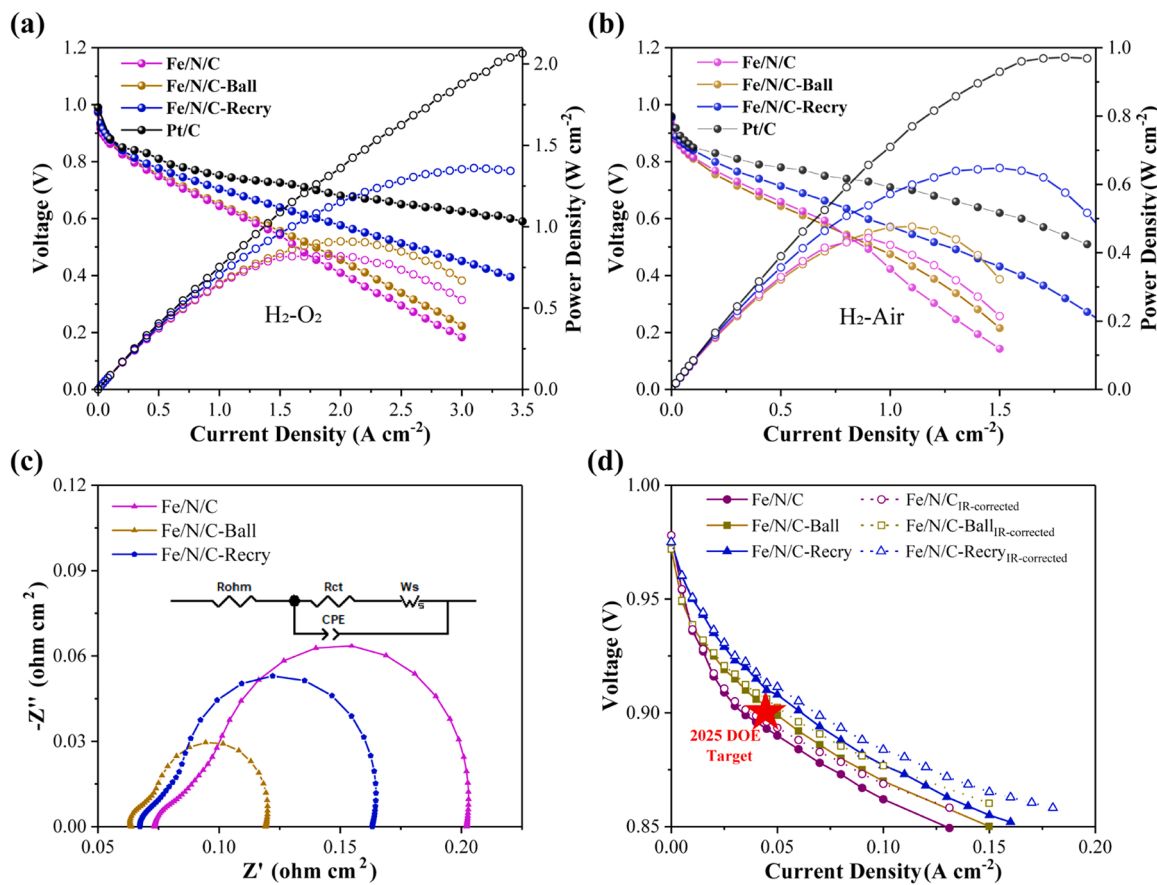


**Fig. 5.** Electrochemical measurements of pyrolysis-derived Fe/N/C catalysts in PEMFCs. (a) H<sub>2</sub>-O<sub>2</sub> and (b) H<sub>2</sub>-air polarization curves with loading of 3 mg<sub>Fe/N/C</sub> cm<sup>-2</sup> and 0.1 mg<sub>Pt</sub> cm<sup>-2</sup> in cathode and anode, respectively. (c) Nyquist plots for H<sub>2</sub>-O<sub>2</sub> PEMFC measured at current density of 1 A cm<sup>-2</sup>. (d) Tafel plots derived from polarization curves with iR-correction in H<sub>2</sub>-O<sub>2</sub> PEMFCs.

rearrangement treatment assists in building Fe/N/C catalysts with more available active sites.

#### 3.4. Practical electrochemical performance evaluated in PEMFCs

Nevertheless, the ORR activities of the catalysts evaluated by rotating disk electrode (RDE) usually can not completely signify their practical application in PEMFCs owing to the dynamical and engineering constraints. Some key parameters such as backpressure, cathodic loading and I/C mass ratio (ionomer/catalyst) play intrinsic roles in the properties of PGM free PEMFCs [36]. Herein, we designed a fine-structured PEMFC with a thin complex membrane (Gore, 15  $\mu$ m) as the proton exchange membrane (PEM) and used 0.1 mg<sub>Pt/C</sub> cm<sup>-2</sup> catalyst coated membrane (CCM)-type anode to diminish the deviation of the PEMFC performance attributed to proton transfer impedance (Fig. S7). In particular, considering a PEM can't withstand a long time of high-temperature (100 °C) baking in the ultrasonic spraying process, a catalyst coated support (CCS)-type cathode deposited with 3 mg<sub>Fe/N/C</sub> cm<sup>-2</sup> catalyst was prepared. Expect the referential pure Pt/C MEA, both the anode and cathode were prepared by CCM-type deposition processes with 0.1 mg<sub>Pt</sub> cm<sup>-2</sup> and 0.2 mg<sub>Pt</sub> cm<sup>-2</sup> catalyst depositions, respectively. After a hot-pressing treatment combined with polyethylene naphthalate seal rings (~80  $\mu$ m), the PGM-free MEA was finished and subsequently sealed into a PEMFC fixture for the following tests. All sealed PEMFCs showed excellent gas tightness with an open voltage of over 0.95 V.

The polarization curves were firstly collected thrice in H<sub>2</sub>-O<sub>2</sub> and subsequently once in H<sub>2</sub>-air (Fig. 5a and b). On account of its dense available active sites and excellent mesoporous structure, the Fe/N/C-

Recry catalyst showed highest peak power densities of 1.36 W cm<sup>-2</sup> and 0.65 W cm<sup>-2</sup> without iR-correction in H<sub>2</sub>-O<sub>2</sub> (300 sccm H<sub>2</sub> and 300 sccm O<sub>2</sub>) and H<sub>2</sub>-air (250 sccm H<sub>2</sub> and 1000 sccm air) fuel cells at 80 °C, 2 bar backpressure and 100% relative humidity (RH), respectively. The corresponding densities of the Fe/N/C were 0.82 W cm<sup>-2</sup> and 0.44 W cm<sup>-2</sup> and the Fe/N/C-Ball were 0.91 cm<sup>-2</sup> and 0.48 W cm<sup>-2</sup>. The polarization curves of the as-prepared Fe/N/C catalysts at a back-pressure of 1 bar were also collected. As shown in Fig. S8, the peak power density of Fe/N/C, Fe/N/C-Ball and Fe/N/C-Recry are 0.71 W cm<sup>-2</sup>, 0.82 W cm<sup>-2</sup> and 1.19 W cm<sup>-2</sup>, respectively. To examine the reliability of excellent performance of the Fe/N/C-Recry catalyst, another PEMFC fixture with an effective area of 5 cm × 5 cm was tested for verification (Fig. S9) and it showed good repeatability.

Nyquist plots were obtained to verify the transfer dynamics of the as-prepared fuel cells (Fig. 5c), in which the value of the initial cross-point intersected with X-axis represents the charge transfer resistance. The results showed that Fe/N/C-Ball exhibited the most favorable charge transfer resistance of 0.064  $\Omega$  cm<sup>-2</sup> owing to its high compaction density, which is attributed to its smaller particle size, compared to the Fe/N/C of 0.073  $\Omega$  cm<sup>-2</sup> and the Fe/N/C-Recry of 0.067  $\Omega$  cm<sup>-2</sup>. The Tafel plots inherited from the polarization curves in Fig. 4a were recorded in detail with iR-correction according to the resistance measurements to further present the catalytic activity of the as-prepared Fe/N/C catalysts in the PEMFCs (Fig. 5d). Favorably, ultra-high current densities of 35 mA cm<sup>-2</sup>, 50 mA cm<sup>-2</sup>, and 63 mA cm<sup>-2</sup> were achieved for Fe/N/C, Fe/N/C-Ball and Fe/N/C-Recry at 0.9 V<sub>iR</sub>-corrected during the first scan in H<sub>2</sub>-O<sub>2</sub>. A breakthrough for the DOE 2025 target for PGM free PEMFCs was achieved using both Fe/N/C-Ball and Fe/N/C-Recry catalysts. To further demonstrate their superior performance, we

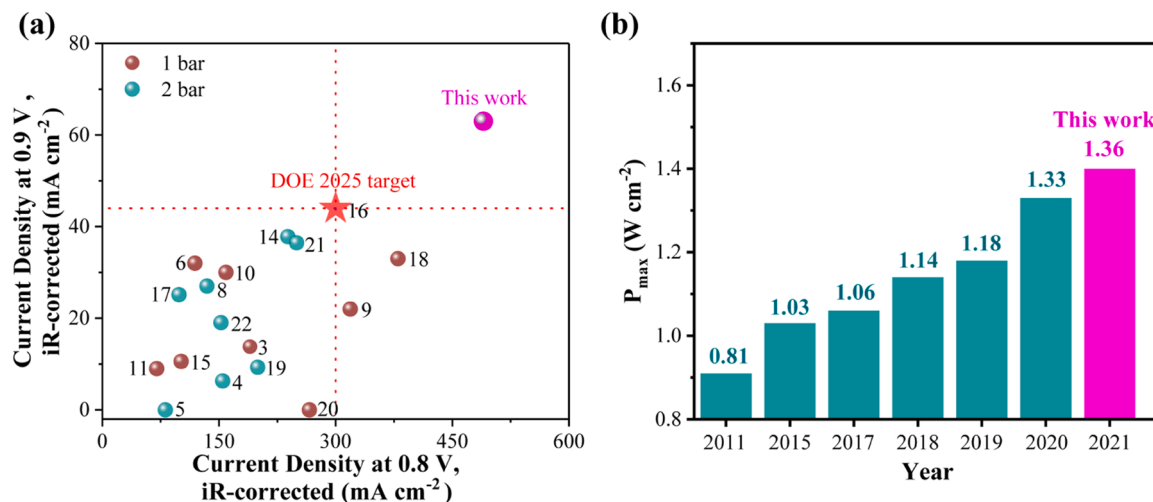


**Fig. 6.** Electrochemical measurements of pyrolysis-derived Fe/N/C catalysts in PEMFCs. (a) H<sub>2</sub>-O<sub>2</sub> and (b) H<sub>2</sub>-air polarization curves with loading of 3 mg<sub>Fe/N/C</sub> cm<sup>-2</sup> and 0.1 mg<sub>Pt</sub> cm<sup>-2</sup> in cathode and anode, respectively. (c) Nyquist plots for H<sub>2</sub>-O<sub>2</sub> PEMFC measured at current density of 1 A cm<sup>-2</sup>. (d) Tafel plots derived from polarization curves with iR-correction in H<sub>2</sub>-O<sub>2</sub> PEMFCs.

marked the outstanding results of PGM-free catalysts over recent years in Fig. 6a and Fig. 6b. It is certain that the Fe/N/C-Recry catalyst sets new records of both high current density output at 0.9 V<sub>iR-free</sub> and peak power density in H<sub>2</sub>-O<sub>2</sub> PEMFCs.

What's more, we collected the polarization curves of the Fe/N/C-Recry cathode catalyst with various loadings in H<sub>2</sub>-O<sub>2</sub> PEMFCs (Fig. S10). The results show that the performance of the fuel cell reaches a peak value when the cathode loading is 3 mg<sub>Fe/N/C</sub> cm<sup>-2</sup>. The stability of the Fe/N/C-Recry catalyst was tested in H<sub>2</sub>-O<sub>2</sub> PEMFCs with the cell voltage holding at 0.7 V (Fig. S11). As reported in most literature work [16,22], the Fe/N/C catalyst prepared here also suffers from severe decay with a current density loss of 75% in the initial 30 h, indicating that further research work is still necessary to improve the poor stability of Fe/N/C catalysts in PEMFCs.

#### 4. Conclusion

We developed an efficient active site rearrangement strategy on the Fe-ZIF precursor, which significantly enhanced the active sites density and mesoporosity of the pyrolysis-derived Fe/N/C catalyst. Consequently, when assembled in PEMFCs, it presented excellent electrochemical performance with new record of peak power density of 1.36 W cm<sup>-2</sup> in H<sub>2</sub>-O<sub>2</sub> and 0.65 W cm<sup>-2</sup> in H<sub>2</sub>-air PEMFCs. Moreover, after iR-corrected, it delivered a favorable current density of 62 mA cm<sup>-2</sup> at 0.9 V in H<sub>2</sub>-O<sub>2</sub> fuel cells, a breakthrough for achieving the DOE 2025 target for PGM-free catalysts. We affirmatively believe that this will accelerate the development of PGM-free catalysts and their practical application in PEMFCs.

#### Funding sources

The authors gratefully acknowledge financial supported by the National Natural Science Foundation of China [21802069].

#### Authors contribution

Sample synthesis, experiment design and exploration were done by Yongkang Wu, Mengchen Yuan, Xiaoke Li, Rui Ding and Xiao Duan. Xiaolin Li and Yunbo Zhang contributed to data analysis. Jia Li, Ying Wang and Jianguo Liu have given important constructive suggestions on this work in terms of idea and the article structure.

#### Declaration of Competing Interest

The authors declare that they have no known competing financial interests or personal relationships that could have appeared to influence the work reported in this paper.

#### Appendix A. Supporting information

Supplementary data associated with this article can be found in the online version at doi:10.1016/j.apcatb.2022.121365.

#### References

- [1] K. Jiao, J. Xuan, Q. Du, Z. Bao, B. Xie, B. Wang, Y. Zhao, L. Fan, H. Wang, Z. Hou, S. Huo, N.P. Brandon, Y. Yin, M.D. Guiver, Designing the next generation of proton-exchange membrane fuel cells, *Nature* 595 (2021) 361–369, <https://doi.org/10.1038/s41586-021-03482-7>.
- [2] X. Qu, Y. Han, Y. Chen, J. Lin, G. Li, J. Yang, Y. Jiang, S. Sun, Stepwise pyrolysis treatment as an efficient strategy to enhance the stability performance of Fe-N/C electrocatalyst towards oxygen reduction reaction and proton exchange membrane fuel cell, *Appl. Catal. B-Environ.* 295 (2021), 120311, <https://doi.org/10.1016/j.apcatb.2021.120311>.
- [3] F. Xiao, Y.C. Wang, Z.P. Wu, G. Chen, F. Yang, S. Zhu, K. Siddharth, Z. Kong, A. Lu, J.C. Li, C.J. Zhong, Z.Y. Zhou, M. Shao, Recent advances in electrocatalysts for proton exchange membrane fuel cells and alkaline membrane fuel cells, *Adv. Mater.* 30 (2021) 2006292, <https://doi.org/10.1002/adma.202006292>.
- [4] X. Ren, Q. Lv, L. Liu, B. Liu, Y. Wang, A. Liu, G. Wu, Current progress of Pt and Pt-based electrocatalysts used for fuel cells, *Sustain. Energy Fuels* 4 (2020) 15–30, <https://doi.org/10.1039/C9SE00460B>.
- [5] S.T. Thompson, D. Papageorgopoulos, Platinum group metal-free catalysts boost cost competitiveness of fuel cell vehicles, *Nat. Catal.* 2 (2019) 558–561, <https://doi.org/10.1038/s41929-019-0291-x>.
- [6] Y. Wang, H. Su, Y. He, L. Li, S. Zhu, H. Shen, P. Xie, X. Fu, G. Zhou, C. Feng, D. Zhao, F. Xiao, X. Zhu, Y. Zeng, M. Shao, S. Chen, G. Wu, J. Zeng, C. Wang, Advanced electrocatalysts with single-metal-atom active sites, *Chem. Rev.* 120 (2020) 12217–12314, <https://doi.org/10.1021/acs.chemrev.0c00594>.
- [7] J. Guo, B. Li, Q. Zhang, Q. Liu, Z. Wang, Y. Zhao, J. Shui, Z. Xiang, Highly accessible atomically dispersed Fe-N<sub>x</sub> sites electrocatalyst for proton-exchange membrane fuel cell, *Adv. Sci.* 8 (2021) 2002249, <https://doi.org/10.1002/advs.202002249>.
- [8] X. Zhao, X. Yang, M. Wang, S. Hwang, S. Karakalos, M. Chen, Z. Qiao, L. Wang, B. Liu, Q. Ma, D.A. Cullen, D. Su, H. Yang, H.-Y. Zang, Z. Feng, G. Wu, Single-iron site catalysts with self-assembled dual-size architecture and hierarchical porosity for proton-exchange membrane fuel cells, *Appl. Catal. B-Environ.* 279 (2020), 119400, <https://doi.org/10.1016/j.apcatb.2020.119400>.
- [9] Z. Chen, X. Liao, C. Sun, K. Zhao, D. Ye, J. Li, G. Wu, J. Fang, H. Zhao, J. Zhang, Enhanced performance of atomically dispersed dual-site Fe-Mn electrocatalysts through cascade reaction mechanism, *Appl. Catal. B-Environ.* 288 (2021), 120021, <https://doi.org/10.1016/j.apcatb.2021.120021>.
- [10] S.T. Thompson, A.R. Wilson, P. Zelenay, D.J. Myers, K.L. More, K.C. Neyerlin, D. Papageorgopoulos, ElectroCat: DOE's approach to PGM-free catalyst and

electrode R&D, *Solid State Ion.* 319 (2018) 68–76, <https://doi.org/10.1016/j.ssi.2018.01.030>.

[11] F. Xiao, X. Liu, C.J. Sun, I. Hwang, Q. Wang, Z. Xu, Y. Wang, S. Zhu, H.W. Wu, Z. Wei, L. Zheng, D. Cheng, M. Gu, G.L. Xu, K. Amine, M. Shao, Solid-state synthesis of highly dispersed nitrogen-coordinated single iron atom electrocatalysts for proton exchange membrane fuel cells, *Nano Lett.* 21 (2021) 3633–3639, <https://doi.org/10.1021/acs.nanolett.1c00702>.

[12] Y. Wang, X.B. Zheng, D.S. Wang, Design concept for electrocatalysts, *Nano Res* 15 (2022) 1730–1752, <https://doi.org/10.1007/s12274-021-3794-0>.

[13] H.Y. Hong, P. Zhu, X.B. Zheng, Z.D. Zhang, D.S. Wang, Y.D. Li, Theory-oriented Screening and Discovery of Advanced Energy Transformation Materials in Electrocatalysis, *Advanced Powder Materials*, <https://doi.org/10.1016/j.apma.2021.10.004>.

[14] X.F. Lu, B.Y. Xia, S.Q. Zang, X.W.D. Lou, Metal-organic frameworks based electrocatalysts for the oxygen reduction reaction, *Angew. Chem. Int. Ed.* 59 (2020) 4634–4650, <https://doi.org/10.1002/anie.201910309>.

[15] Y. Wang, D. Wang, Y. Li, Rational design of single-atom site electrocatalysts: from theoretical understandings to practical applications, *Adv. Mater.* 33 (2021), e2008151, <https://doi.org/10.1002/adma.202008151>.

[16] Y. Deng, J. Luo, B. Chi, H. Tang, J. Li, X. Qiao, Y. Shen, Y. Yang, C. Jia, P. Rao, S. Liao, X. Tian, Advanced atomically dispersed metal–nitrogen–carbon catalysts toward cathodic oxygen reduction in PEM fuel cells, *Adv. Energy Mater.* 11 (2021) 2101222, <https://doi.org/10.1002/aenm.202101222>.

[17] H. Zhang, H.T. Chung, D.A. Cullen, S. Wagner, U.I. Kramm, K.L. More, P. Zelenay, G. Wu, High-performance fuel cell cathodes exclusively containing atomically dispersed iron active sites, *Energy Environ. Sci.* 12 (2019) 2548–2558, <https://doi.org/10.1039/C9EE00877B>.

[18] X. Wang, Y. Jia, X. Mao, D. Liu, W. He, J. Li, J. Liu, X. Yan, J. Chen, L. Song, A. Du, X. Yao, Edge-rich Fe–N<sub>4</sub> active sites in defective carbon for oxygen reduction catalysis, *Adv. Mater.* 32 (2020), e2000966, <https://doi.org/10.1002/adma.202000966>.

[19] Q. Wang, Y. Yang, F. Sun, G. Chen, J. Wang, L. Peng, W.T. Chen, L. Shang, J. Zhao, D. Sun-Waterhouse, T. Zhang, G.I.N. Waterhouse, Molten NaCl-assisted synthesis of porous Fe–N–C electrocatalysts with a high density of catalytically accessible FeN<sub>4</sub> active sites and outstanding oxygen reduction reaction performance, *Adv. Energy Mater.* 11 (2021) 2100219, <https://doi.org/10.1002/aenm.202100219>.

[20] M. Mazzucato, G. Daniel, A. Mahmood, T. Kosmala, G. Granozzi, A. Kucernak, C. Durante, Effects of the induced micro- and meso-porosity on the single site density and turn over frequency of Fe–N–C carbon electrodes for the oxygen reduction reaction, *Appl. Catal. B-Environ.* 291 (2021), 120028, <https://doi.org/10.1016/j.apcatb.2021.120068>.

[21] X. Wan, X. Liu, Y. Li, R. Yu, L. Zheng, W. Yan, H. Wang, M. Xu, J. Shui, Fe–N–C electrocatalyst with dense active sites and efficient mass transport for high-performance proton exchange membrane fuel cells, *Nat. Catal.* 2 (2019) 259–268, <https://doi.org/10.1038/s41929-019-0237-3>.

[22] Y. Li, P. Zhang, L. Wan, Y. Zheng, X. Qiu, H. Zhang, Y. Wang, K. Zaghib, J. Yuan, S. Sun, Y. Wang, Z. Zhou, S. Sun, A general carboxylate-assisted approach to boost the ORR performance of ZIF-Derived Fe/N/C catalysts for proton exchange membrane fuel cells, *Adv. Funct. Mater.* 31 (2021) 2009645, <https://doi.org/10.1002/adfm.202009645>.

[23] L. Jiao, J. Li, L.L. Richard, Q. Sun, T. Stracensky, E. Liu, M.T. Sougrati, Z. Zhao, F. Yang, S. Zhong, H. Xu, S. Mukerjee, Y. Huang, D.A. Cullen, J.H. Park, M. Ferrandon, D.J. Myers, F. Jaouen, Q. Jia, Chemical vapour deposition of Fe–N–C oxygen reduction catalysts with full utilization of dense Fe–N<sub>4</sub> sites, *Nat. Mater.* 20 (2021) 1385–1391, <https://doi.org/10.1038/s41563-021-01030-2>.

[24] M. Primbs, Y. Sun, A. Roy, D. Malko, A. Mahmood, M.-T. Sougrati, P.-Y. Blanchard, G. Granozzi, T. Kosmala, G. Daniel, P. Atanassov, J. Sharman, C. Durante, A. Kucernak, D. Jones, F. Jaouen, P. Strasser, Establishing reactivity descriptors for platinum group metal (PGM)-free Fe–N–C catalysts for PEM fuel cells, *Energy Environ. Sci.* 13 (2020) 2480–2500, <https://doi.org/10.1039/D0EE01013H>.

[25] D. Malko, A. Kucernak, T. Lopes, Performance of Fe–N/C oxygen reduction electrocatalysts toward NO<sub>2</sub>(·), NO, and NH<sub>2</sub>OH electroreduction: from fundamental insights into the active center to a new method for environmental nitrite destruction, *J. Am. Chem. Soc.* 138 (2016) 16056–16068, <https://doi.org/10.1021/jacs.6b09622>.

[26] S. Wang, T. Dai, Y. Lu, Q. Chen, L. Feng, Z. Sui, Fullerene-bearing porous polymer via ball-milling approach and its palladium composite for catalytic deallylation, *Microporous Mesoporous Mater.* 302 (2020), 110187, <https://doi.org/10.1016/j.micromeso.2020.110187>.

[27] C.H. Choi, C. Baldizzone, J.P. Grote, A.K. Schuppert, F. Jaouen, K.J. Mayrhofer, Stability of Fe–N–C catalysts in acidic medium studied by operando spectroscopy, *Angew. Chem. Int. Ed.* 54 (2015) 12753–12757, <https://doi.org/10.1002/anie.201504903>.

[28] G. Lu, S. Li, Z. Guo, O.K. Farha, B.G. Hauser, X. Qi, Y. Wang, X. Wang, S. Han, X. Liu, J.S. DuChene, H. Zhang, Q. Zhang, X. Chen, J. Ma, S.C. Loo, W.D. Wei, Y. Yang, J.T. Hupp, F. Huo, Imparting functionality to a metal–organic framework material by controlled nanoparticle encapsulation, *Nat. Chem.* 4 (2012) 310–316, <https://doi.org/10.1038/NCHEM.1272>.

[29] I.G. Filippova, Y.A. Simonov, M. Gdanets, V. Stavila, Crystal structure of tris (1,10-phenanthroline) iron (II) dinitrate dihydrate, *J. Struct. Chem.* 46 (2005) 1095–1098, <https://doi.org/10.1007/s10947-006-0249-0>.

[30] J. Li, L. Jiao, E. Wegener, L.L. Richard, E. Liu, A. Zitolo, M.T. Sougrati, S. Mukerjee, Z. Zhao, Y. Huang, F. Yang, S. Zhong, H. Xu, A.J. Kropf, F. Jaouen, D.J. Myers, Q. Jia, Evolution pathway from iron compounds to Fe<sub>1</sub>(II)–N<sub>4</sub> sites through gas-phase iron during pyrolysis, *J. Am. Chem. Soc.* 142 (2020) 1417–1423, <https://doi.org/10.1021/jacs.9b11197>.

[31] J. Han, H. Bao, J.-Q. Wang, L. Zheng, S. Sun, Z.L. Wang, C. Sun, 3D N-doped ordered mesoporous carbon supported single-atom Fe–N–C catalysts with superior performance for oxygen reduction reaction and zinc-air battery, *Appl. Catal. B-Environ.* 280 (2021), 119411, <https://doi.org/10.1016/j.apcatb.2020.119411>.

[32] H. Xu, D. Wang, P. Yang, L. Du, X. Lu, R. Li, L. Liu, J. Zhang, M. An, A hierarchically porous Fe–N–C synthesized by dual melt-salt-mediated template as advanced electrocatalyst for efficient oxygen reduction in zinc-air battery, *Appl. Catal. B-Environ.* 303 (2022), 121040, <https://doi.org/10.1016/j.apcatb.2021.121040>.

[33] J. Yan, X. Han, J. Qian, J. Liu, X. Dong, F. Xi, Preparation of 2D graphitic carbon nitride nanosheets by a green exfoliation approach and the enhanced photocatalytic performance, *J. Mater. Sci.* 52 (2017) 13091–13102, <https://doi.org/10.1007/s10853-017-1419-5>.

[34] J. Li, M.T. Sougrati, A. Zitolo, J.M. Ablett, I.C. Oğuz, T. Mineva, I. Matanovic, P. Atanassov, Y. Huang, I. Zenyuk, A. Di Cicco, K. Kumar, L. Dubau, F. Maillard, G. Dražić, F. Jaouen, Identification of durable and non-durable FeN<sub>x</sub> sites in Fe–N–C materials for proton exchange membrane fuel cells, *Nat. Catal.* 4 (2020) 10–19, <https://doi.org/10.1038/s41929-020-00545-2>.

[35] A. Zitolo, V. Goellner, V. Armel, M.T. Sougrati, T. Mineva, L. Stievano, E. Fonda, F. Jaouen, Identification of catalytic sites for oxygen reduction in iron- and nitrogen-doped graphene materials, *Nat. Mater.* 14 (2015) 937–942, <https://doi.org/10.1038/NMAT4367>.

[36] R. Ding, R. Wang, Y. Ding, W. Yin, Y. Liu, J. Li, J. Liu, Designing AI-aided analysis and prediction models for nonprecious metal electrocatalyst-based proton-exchange membrane fuel cells, *Angew. Chem. Int. Ed.* 59 (2020) 19175–19183, <https://doi.org/10.1002/anie.202006928>.